

# SCIENTIFIC REPORTS



OPEN

## MOF-derived multifractal porous carbon with ultrahigh lithium-ion storage performance

Ang Li<sup>1</sup>, Yan Tong<sup>1</sup>, Bin Cao<sup>1</sup>, Huaihe Song<sup>1</sup>, Zhihong Li<sup>2</sup>, Xiaohong Chen<sup>1</sup>, Jisheng Zhou<sup>1</sup>, Gen Chen<sup>3</sup> & Hongmei Luo<sup>3</sup>

Received: 21 October 2016

Accepted: 08 December 2016

Published: 11 January 2017

Porous carbon is one of the most promising alternatives to traditional graphite materials in lithium-ion batteries. This is not only attributed to its advantages of good safety, stability and electrical conductivity, which are held by all the carbon-based electrodes, but also especially ascribed to its relatively high capacity and excellent cycle stability. Here we report the design and synthesis of a highly porous pure carbon material with multifractal structures. This material is prepared by the vacuum carbonization of a zinc-based metal-organic framework, which demonstrates an ultrahigh lithium storage capacity of 2458 mAh g<sup>-1</sup> and a favorable high-rate performance. The associations between the structural features and the lithium storage mechanism are also revealed by small-angle X-ray scattering (SAXS), especially the closed pore effects on lithium-ion storage.

The increasing demands for high-performance power batteries have gained a sustained research and development in lithium-ion battery electrodes<sup>1,2</sup>. Up to date, several mechanisms of lithium storage in pure carbon materials have been proposed, which can be roughly classified into three types according to the lithium embedded position: the intercalation into graphite layer structures, the storage at interfaces and surfaces and the storage in defects with different dimensionality<sup>3</sup>. The disordered carbons derived from certain polymers can provide an excess storage capacity by the additional bulk intercalation of lithium atoms, which corresponds to the formation of Li<sub>2</sub>C<sub>6</sub> and Li<sub>3</sub>C<sub>6</sub>. The presence of covalent Li<sub>2</sub> molecules<sup>3,4</sup> is usually used to explain the unexpected high capacity for bulk storage (even up to 1116 mAh g<sup>-1</sup>). In some reports, the models of “house of cards” and “falling cards” were proposed to explain the extra lithium ion storage at the external and internal interfaces of the disordered carbons<sup>5,6</sup>. Surface stored lithium can be treated as an intermediate state between intercalated lithium and metallic lithium, which achieves by the occupancy of various lithium sites to form lithium multilayers on the surface of carbon<sup>7</sup>. Another important mechanism considering the constructive role of defects<sup>3</sup> is of the view that the microstructures, like cavities, nanopores and vacancies, can also bring an extra capacity<sup>8,9</sup>. The pore-filling model presumes that the pores in the carbon materials, if small enough, will be filled with adsorbed lithium atoms<sup>8</sup>. These nanopores will be accommodated by clusters of lithium atoms in which the bond is weaker than that in metallic lithium, while solvent molecules cannot enter the pores. An interesting phenomenon in this model is that the closed pores are accessible for lithium with fast permeability but not for N<sub>2</sub> molecules, which makes lithium storage sites of this type cannot be characterized by N<sub>2</sub> sorption method<sup>3</sup>; therefore, there are still no experimental evidence to support such an instructive viewpoint. For all the aforementioned mechanisms, the structures of carbon materials, which depend mainly on the types of precursors and conditions of pyrolysis, have a great effect on the lithium storage modes<sup>10</sup>.

In order to break through the limitation of the intercalation capacity of the commercial graphite materials (372 mAh g<sup>-1</sup>) and the organic precursor-derived carbon, significant efforts have been made to design novel materials to enhance the reversible lithium storage capacity by increasing the degree of lattice disorder, enlarging surface area and increasing defect density<sup>3,11,12</sup>. Porous carbon can satisfy these structural requirements almost simultaneously<sup>11</sup>. In recent years, a kind of porous carbon materials which have hierarchical pore structures with

<sup>1</sup>State Key Laboratory of Chemical Resource Engineering, Beijing Key Laboratory of Electrochemical Process and Technology for Materials, Beijing University of Chemical Technology, Beijing, 100029, P. R. China. <sup>2</sup>Beijing Synchrotron Radiation Facility, Institute of High Energy Physics, Chinese Academy of Sciences, 19B Yuquan Road, Beijing 100049, P. R. China. <sup>3</sup>Department of Chemical and Materials Engineering, New Mexico State University, Las Cruces, New Mexico 88003, United States. Correspondence and requests for materials should be addressed to H.S. (email: songhh@mail.buct.edu.cn)

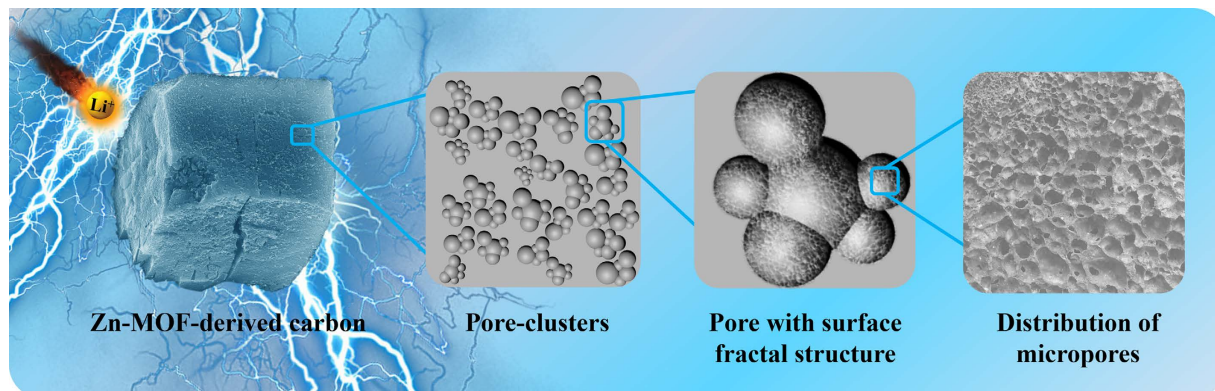


**Figure 1.** Schematic illustration of the multifractal structure of MOF-derived porous carbon (FPC and VFPC).

a broad pore size distribution have been designed to optimize the conditions for electrolyte permeation and lithium accommodation, which are aroused tremendous interest<sup>13</sup>. These hierarchical porous carbon materials exhibit an enhanced electrochemical performance than the traditional porous carbon materials<sup>14</sup>. Inspired by the concepts of fractal structure and hierarchical pore size distribution, the structure design of porous carbon, by organizing the hierarchical pores into porous and surface fractal structures, can be introduced to take full advantage of all the lithium storage modes<sup>15</sup>.

Metal-organic frameworks (MOFs) are a kind of promising precursors for porous carbon preparation, due to their tunable ordered porous structures and compositions<sup>2,16–18</sup>. Many works prepared porous carbon from MOFs for the applications in supercapacitors<sup>19–21</sup>, lithium-sulfur batteries<sup>22,23</sup>, oxygen reduction reactions<sup>19,24–26</sup>, as well as lithium-ion batteries (LIBs)<sup>2,27–30</sup>. Their highly porous structures and heteroatom effects have led to unexpected performances in these fields. However, as electrodes for LIBs, most reports concentrated on introducing heteroatoms to enhance the lithium storage performance, rather than the structure design and architecture assembly. This study aims to design and prepare hierarchical porous carbon materials with multifractal structures for high-performance LIBs by varying the conditions of the precursor pyrolysis process. The relationships between the structural features and the lithium storage mechanisms are also investigated. In addition, the important role of closed pores in lithium storage will be revealed by a comprehensive analysis of porous properties of products using synchrotron radiation small-angle X-ray scattering (SAXS).

## Results and Discussion

A Zn-based MOF (Zn-MOF) with terephthalic acid as ligand was used as precursor, which exhibits a high Brunauer-Emmet-Teller (BET) specific surface area and a relatively wide pore size distribution (see Supplementary SI.1). A simply thermal treatment was used to design and prepare porous carbon with multifractal structures, as illustrated in Fig. 1, by varying the pyrolytic pressure. After pyrolysis, both of the products have maintained the original morphology of the shape of Zn-MOF grains (Fig. 2 for products; Fig. S1c & d for precursor); however, the surfaces of the products are cavernous. As can be seen in Fig. 2, the pores and cavities in the sample pyrolyzed in vacuum (VFPC) are smaller and denser than those of the sample pyrolyzed under normal pressure (FPC), and all the pores and cavities are globulous and interconnected. The results of XRD and EDS show that both FPC and VFPC are amorphous carbon (Fig. S2 for EDS; Fig. S3a for XRD). XRD patterns of FPC and VFPC both display two weak diffraction peaks at  $2\theta = 23.7^\circ$  and  $43.9^\circ$ , corresponding to (002) and (100) reflections of carbon, respectively. None of the original ordered porous structures in Zn-MOF are maintained after the pyrolysis process, implying the collapse of carbon skeletons. VFPC shows a higher purity of carbon but a lower carbon yield based on MOF precursor (VFPC, 2.19%; FPC, 2.26%), indicating that the vacuum atmosphere can improve the gasification reactions and purify the carbon materials. In Raman spectroscopy (Fig. S3b), the characteristic peaks are typically indicated to elemental carbon. The band intensity ratio of  $I_D/I_G$  for the D band and the G band is a significant and widely used factor to quantify the disorder degree of carbon materials<sup>2</sup>. Based on the data in Fig. S3b, we can calculate that the  $I_D/I_G$  for FPC and VFPC are 1.14 and 1.11, respectively. It can be concluded that the disordered structure in FPC is higher than that in VFPC. The microstructures of samples were investigated by HRTEM in detail, as illustrated in Fig. 3a–d. Both FPC and VFPC show a porous structure, and their local magnification pictures displayed in Fig. 3c,d show a typical characteristic of amorphous carbon with random and disordered lattice fringes. The surface of VFPC is more irregular than that of FPC, which might be ascribed to the strong etching effect and pyrolysis process in vacuum.

The pore properties of the two samples were investigated by two techniques independently:  $N_2$  sorption and SAXS. The  $N_2$  adsorption isotherms of the two samples both illustrate characteristics of type IV (Fig. 4a,b), indicating the existence of mesopores<sup>31</sup>. The rapid uptake of adsorption curves at low relative pressure range ( $P/P_0 < 0.1$ ) is ascribed to the adsorption of  $N_2$  in micropores<sup>31</sup>. As illustrated in Table 1, the BET specific surface area ( $S_{BET}$ ) and pore volume ( $V$ ) of VFPC show slight bigger values than those of FPC, while the micropore volume ( $V_{mic}$ ) of VFPC is smaller. The pore size distributions of both samples, simulated by non-local density functional theory (NLDFT) model, show a wide distribution in the range of micropores and mesopores, indicating

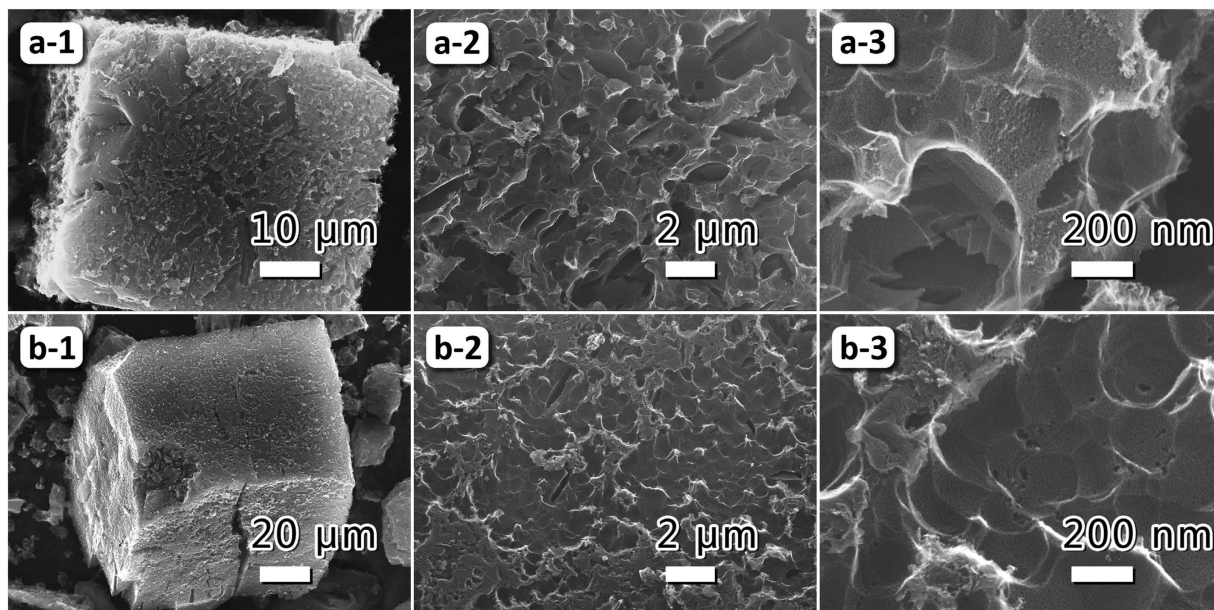


**Figure 2.** Morphology characterizations of FPC and VFPC by SEM. (a) and (b) are images of FPC and VFPC, respectively.

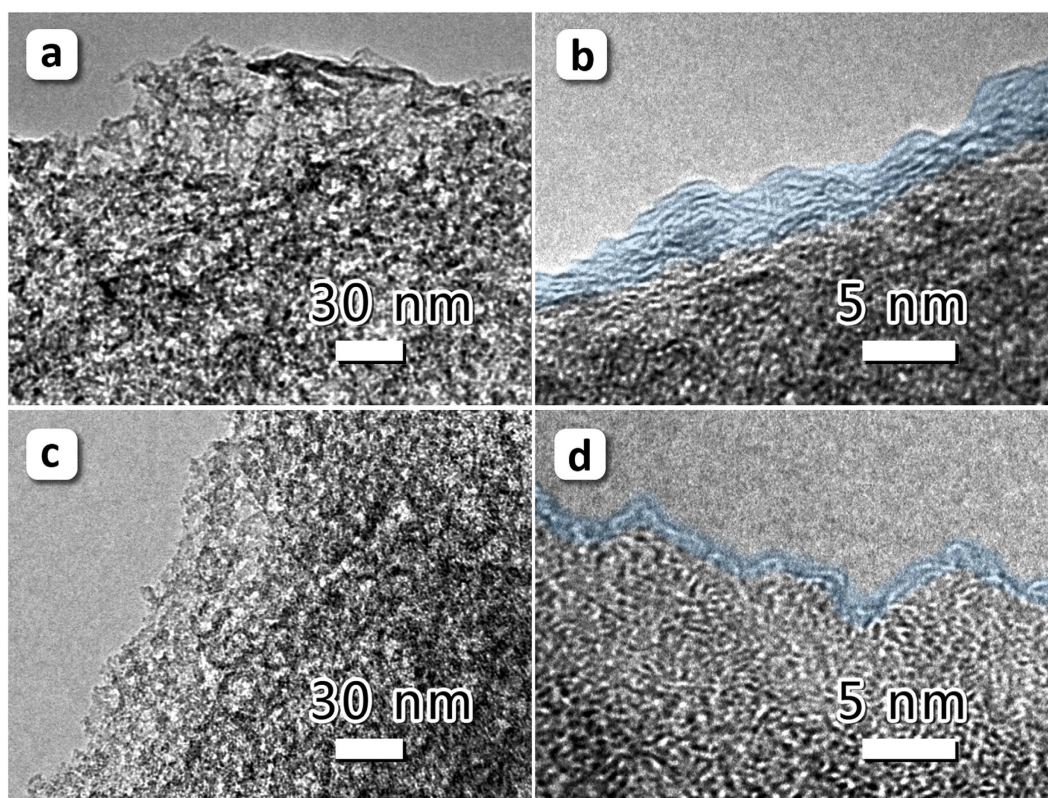


**Figure 3.** Microstructural characterization of FPC and VFPC. (a,b) and (c,d) are HRTEM images of FPC and VFPC, respectively. No obvious ordered structure can be found, indicating the formation of amorphous carbon. As highlighted in blue in (b) and (d), VFPC shows a more irregular surface structure than that of FPC.

a hierarchical porous structure (Fig. 4c). The average pore size of VFPC and FPC simulated by BET method are 4.41 nm and 4.31 nm, respectively.

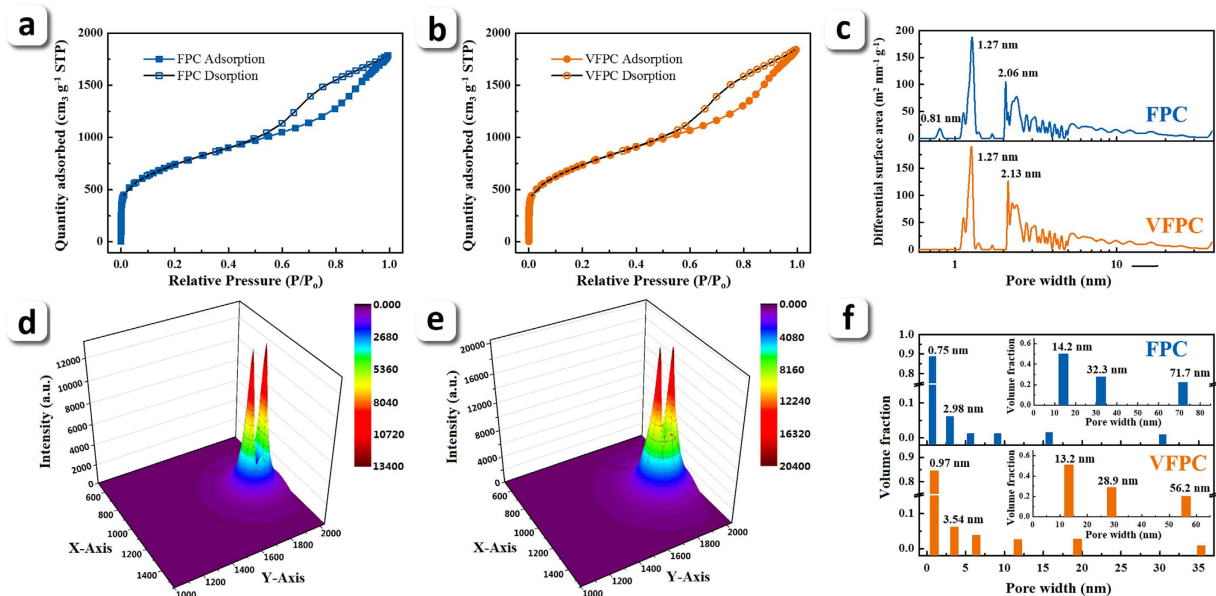


**Figure 4.** Porous property characterizations of FPC and VFPC. (a) and (b) are  $N_2$  adsorption isotherms of FPC and VFPC, respectively; (c) is the pore size distribution of the samples. (d) and (e) are 2D SAXS pattern with transmitted intensity as a Z-axis for FPC and VFPC, respectively. The color bars are the scaling of intensity. (f) Is the pore size distribution of the samples, which was determined by a cascade tangent rule of Jellinek method (Fig. S3). The insets in (f) are the pore size distribution of the fully lithiated samples, respectively.

Materials	$S_{BET}^a$	$V^b$	$V_{mic}^c$	$S_{SAXS}$	$V_{SAXS}$	$V_{mic}^{SAXS}$	$\Delta S^d$	$\Delta V_{mic}^d$
FPC	2565	2.76	0.14	2826	3.91	0.41	261	0.27
VFPC	2587	2.85	0.09	3125	3.82	0.40	538	0.31

**Table 1.** The porous properties from SAXS and  $N_2$  sorption experiments for FPC and VFPC.  $N_2$  sorption method:  $S_{BET}$ -specific surface area ( $m^2 g^{-1}$ );  $V$  - total pore volume ( $cm^3 g^{-1}$ );  $V_{mic}$ -micropore volume ( $cm^3 g^{-1}$ ). SAXS method:  $S_{SAXS}$ -specific surface area ( $m^2 g^{-1}$ );  $V_{SAXS}$  - total pore volume ( $cm^3 g^{-1}$ );  $V_{mic}^{SAXS}$  micropore volume ( $cm^3 g^{-1}$ ). <sup>a</sup>Calculated by BET method. <sup>b</sup>Calculated from the adsorbing capacity when  $P/P_0 = 0.995$ . <sup>c</sup>Calculated by t-plot method. <sup>d</sup> $\Delta S = S_{SAXS} - S_{BET}$  ( $m^2 g^{-1}$ );  $\Delta V_{mic} = V_{mic}^{SAXS} - V_{mic}$  ( $cm^3 g^{-1}$ ).

Further investigation was performed by SAXS to confirm the pore structure of the samples, including the properties of open pores and closed pores (Fig. 4d–f). The removal of the scattering background and the normalization of the scattering intensity have been made to correct the primary data. The specific surface area ( $S_{SAXS}$ ) from SAXS data can be obtained by the Porod's law and the invariant (Fig. S4)<sup>32</sup>. The results show that the  $S_{SAXS}$  of FPC and VFPC are 2870 and 3125  $m^2 g^{-1}$ , respectively. Significantly, the values of  $S_{SAXS}$  for both samples, especially for VFPC, are larger than those of  $S_{BET}$  obtained by  $N_2$  sorption method. Such phenomenon could be attributed to the constrictions that hinder the diffusion of  $N_2$  molecules, in some parts of closed pores and blind pores, or the open micropores that are too narrow to accommodate two layers of  $N_2$  molecules<sup>33</sup>. The average pore size of VFPC is 2.12 nm, which is still bigger than that of FPC (1.55 nm). The pore size distributions of the two samples from SAXS method also display hierarchical characteristics, as shown in the NLDFT results; however, the contribution of micropores to the total pore volume that calculated by the SAXS method is much higher than the results from  $N_2$  sorption method (Table 1, see Supplementary SI.3 & 4 for calculation details). As illustrated in Fig. 4f, the contributions of micropores to  $S_{SAXS}$  for FPC and VFPC are almost all the super-micropores ( $< 1$  nm). The most probable pore sizes of FPC and VFPC are 0.75 and 0.97 nm, respectively, which occupy the most of the scatterer volume, indicating the existence of a large amount of super-micropores that cannot be detected by  $N_2$  sorption. Across the two samples, considering the results of  $N_2$  sorption method and Raman spectra, we can conclude that the vacuum carbonization will expand the specific surface areas of the products, especially the contribution from micropores, and enlarge the average pore sizes but decrease the disordered degree of carbon.

Irregular geometric structures are also characteristics of the samples, which can be quantified by the fractal analysis with SAXS method<sup>32</sup>. The SAXS intensity from fractal samples obeys a power-law form,  $I = I_0 q^{-\alpha}$ , where  $\alpha$  can be used to determine the fractal type and dimensions (Fig. S5)<sup>32</sup>. The analysis shows two types of fractal structures in the samples, porous fractal and surface fractal. The porous fractal behavior of both FPC and VFPC can be characterized by porous fractal dimension  $D_p$ .  $D_p$  are 2.70 and 2.19 for FPC and VFPC, respectively, and the higher  $D_p$  means a larger degree of inhomogeneity in porous distribution of the two samples<sup>32</sup>. Moreover, the surface fractal behavior is observed and characterized by surface fractal dimension  $D_s$ .  $D_s$  are 2.39 and 2.86 for FPC and VFPC, respectively. The surface irregularities of the two samples also can be confirmed in their HRTEM

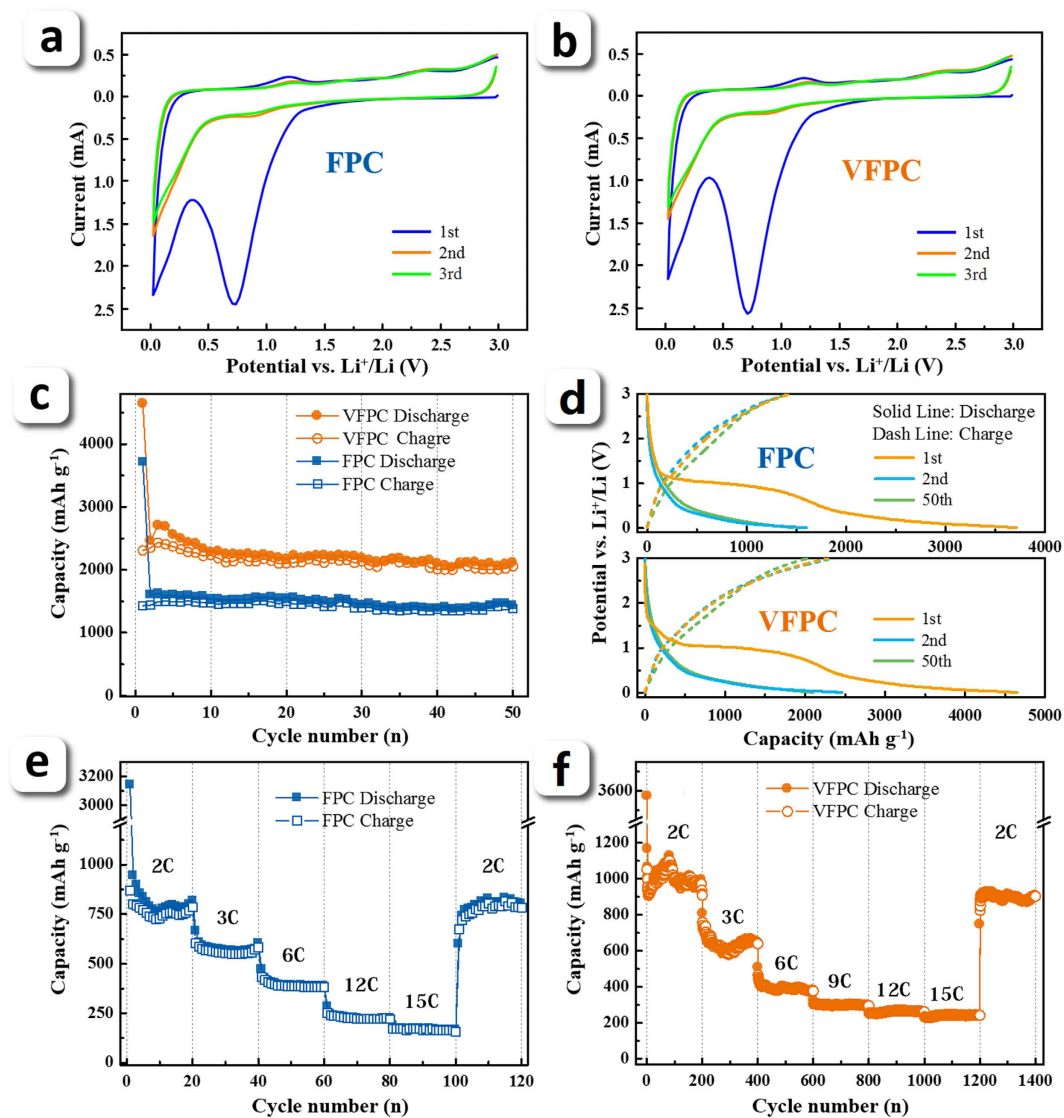


**Figure 5. Electrochemical performance of FPC and VFPC.** (a) Cycle performances of the samples at 0.2C. (b) Is Galvanostatic charge-discharge profiles at 0.2C with a voltage range between 0.01 and 3.0V for the 1st, the 2nd and the 50th cycle of FPC and VFPC, respectively; (c) and (d) are high-rate performances of FPC and VFPC at each rate, respectively. (e) and (f) are CV curves of FPC and VFPC, respectively.

pictures in Fig. 3a–d. The bigger value of  $D_s$  of VFPC reveals a more irregular and rougher surface structure<sup>34</sup>. In addition, the  $\ln I - \ln q$  curve of VFPC exhibits a surplus of surface fractal behavior, indicating a surface fractal geometric structure in a different scale. The VFPC shows a multifractal behavior in the organization of its hierarchical pores, suggesting that the vacuum pyrolysis can lead to more complex fractal structures.

Combining the results of SEM, SAXS and  $N_2$  sorption method, one can get a clear information on the porous structure of the samples. As illustrated in Fig. 1, the porous system is made up of “pore clusters” which are mainly comprised of mesopores. This is reflected as a porous fractal behavior in SAXS analysis. Most of the micropores are distributed on the surface of pores in “pore clusters” densely. The VFPC even shows a surface bi-fractal behavior in the distribution of its micropores.

Electrochemical performances of the as-products were measured with a two-electrode coin-type cell with lithium foil as counter electrode. The cyclic voltammetry (CV) results of the two samples show a typical porous carbon lithiation appearance (Fig. 5a,b). The first (0.01–0.3 V) and second (0.5–1.0 V) peaks can be attributed to the Li-insertion into carbon matrix, and the lithium ion storage on surface, respectively<sup>2,3</sup>. As can be seen in Fig. 5c, the first reversible capacity (Li-desertion) of FPC is 1600  $\text{mAh g}^{-1}$ , and that of VFPC even reaches as high as 2458  $\text{mAh g}^{-1}$  at 0.2 C ( $1C = 370 \text{ mA g}^{-1}$ ). After 50 cycles, the reversible capacity of VFPC is still at 2016  $\text{mAh g}^{-1}$ . The charge-discharge profiles in Fig. 5d show a plateau at approximately 1 V in 1st cycle which can be ascribed to the formation of SEI film on the electrode surfaces<sup>2</sup>, and the contribution of reversible capacity mainly occurs under 0.5 V. The cyclic voltammetry results of the two samples are consistent with charge-discharge profiles very well (Fig. 5a–d). Durable cycle life of FPC and VFPC at high rate is also obtained (Fig. 5e,f). The

reversible capacity of VFPC at 2C is 1012 mAh g<sup>-1</sup>, which is ca. 50% of that at 0.2C. Even at a rate of 15C, a reversible capacity of 245 mAh g<sup>-1</sup> is still maintained, and the tests show an excellent cyclic stability at each rate. For the first time, the fractal structure is used in porous carbon design for lithium storage, which can improve the lithium storage performance dramatically. The fractal porous structure can provide favorable high-rate performance and excellent cyclic stability by adjusting the pore spatial distribution in carbon matrix without introducing any other heteroatoms. To the best of our knowledge, the outstanding performance of VFPC is not only better than those of other porous pure carbon materials as provided in the literatures (Table S1), but also comparable with other kinds of carbon-based anode materials like carbon nanotubes, heteroatom-doped porous carbon, graphene and their composites, etc.<sup>35–37</sup>.

The FPC and VFPC in fully lithium intercalation state (denoted as Li-FPC and Li-VFPC, respectively) were also investigated by SAXS method. The Porod analysis of both Li-FPC and Li-VFPC shows a negative deviation (Fig. S6), indicating the existence of a transition zone, i.e., an interface layer, between two phases without sharp boundary<sup>32,38</sup>. The values of average thickness of the transition zone are 1.97 and 2.37 nm for Li-FPC and Li-VFPC, respectively, which were determined by the correction process of negative deviation. Considering the absence of micropores in both Li-FPC and Li-VFPC (insets in Fig. 4f), we speculate that all the micropores are fully filled by lithium atoms, as the electrolyte molecules are too large to embed into such small micropores. Therefore, we consider that the transition zone is comprised of solid electrolyte interface (SEI) film and surface defects filled by lithium, while the bulk phase is comprised of lithium carbides and lithium-embedded micropores. The electron densities ( $\rho_e$ ) of the two phases and the transition zone can be calculated from Porod constant (see Supplementary SI6)<sup>38</sup>. As the scattering background has been removed, the electron density of the pore phase can be treated as zero, and the electron density difference of the two phase can be regarded as the electron density of the bulk phase ( $\rho_e^b$ ). By comparing with other reported electrochemical lithium intercalation carbon products (see Supplementary SI6 and Table S2), the  $\rho_e^b$  of Li-FPC is 1.101 mol cm<sup>-3</sup> which can be deemed as a bulk storage with  $x = 1–1.5$  in Li<sub>x</sub>C<sub>6</sub>, and 1.132 mol cm<sup>-3</sup> of Li-VFPC can be deemed as a bulk storage with  $x = 1.5–2$  in Li<sub>x</sub>C<sub>6</sub>. The average  $\rho_e$  of transition zones are 0.551 and 0.566 mol cm<sup>-3</sup> for Li-FPC and Li-VFPC, respectively, and these low  $\rho_e$  might be ascribed to the surface storage and defect storage of lithium atoms. It can be seen that the higher surface fractal dimension and the larger closed pore volume can lead to more lithium storage in both surface and bulk storage modes.

From the data analysis above, it can be found that both of the fractal structures and the pores that cannot be detected by N<sub>2</sub> sorption method have played an dramatic role in lithium storage in carbon materials. According to the theory of electrochemical reaction on fractal surface, surface or interface with higher surface fractal dimension can provide larger electrochemical active surface area and smaller internal resistance<sup>39,40</sup>. The VFPC with a higher surface fractal dimension exhibits a better electrochemical performance due to the enhanced surface storage mode that has been proved by the transition zone analysis using SAXS method. The electrochemical impedance spectra (EIS) analysis of FPC and VFPC have also shown that higher surface fractal dimension leads to a lower charge transfer resistance (see Fig. S7 and Table S3). The electrochemical reactions occurring on the surface and interface were also strengthened by the larger  $\Delta S$  and  $D_s$ , which led to a stronger peak in CV plot at around 0.7 V as can be seen in Fig. 5a,b. As the surface and interface with higher  $D_s$  can provide higher electrochemical active site density, the larger specific surface area will provide much more active sites for the lithiation reactions. This view point is also proved by the EIS results with a lower charge transfer resistance indicating a better ionic diffusion in VFPC (see Table S3). The surface storage of Li in carbon was proved by TEM results which show a uniform dispersion of Li<sub>2</sub>O, and the statistical results also illustrate the advantage of surface fractal structure (see Supplementary SI8 and Fig. S8). The morphology images of FPC and VFPC after 50 charge-discharge cycles show the stabilizing effect of surface fractal structure by displaying a more smooth surface of VFPC (see Fig. S9). If we regard  $\Delta S$  and  $\Delta V_{mic}$  as specific surface area and micropore volume that cannot be detected by N<sub>2</sub> sorption method, it can be found that VFPC prepared by vacuum pyrolysis can provide a larger  $\Delta S$  and  $\Delta V_{mic}$ , which finally achieve an ultrahigh lithium storage performance. After lithium intercalation, the micropores disappeared (Fig. 4f), and the  $S_{SAXS}$  of FPC and VFPC fell to 110 and 103 m<sup>2</sup> g<sup>-1</sup>, respectively, which could be attributed to the filling of micropores by lithium atoms and the formation of the relatively thick transition zones. In addition, the higher intercalation degree of bulk storage in VFPC is also illustrative of the important roles of surface fractal structures,  $\Delta S$  and  $\Delta V_{mic}$  in promoting the lithium storage performance by different storage modes.

## Conclusion

In conclusion, the fractal structures of porous carbon, as well as the pores that cannot be detected by N<sub>2</sub> sorption method, advance the lithium storage capacity dramatically by enhancing the bulk storage, surface storage and defect storage. The vacuum pyrolysis process can induce the formation of multi-fractal structure of porous carbon and more closed pores. The macropores and mesopores offer short path of lithium ions by optimizing the conditions for electrolyte penetration. Subnanopores distributed with fractal structures can provide a large amount of lithium storage active sites, which may generate a transition zone rich in lithium atoms. We believe that the idea of the fractal structures and the closed pore storage mode can be introduced into the design of electrodes for other metal-ion batteries and energy storage devices.

## Methods

**Synthesis of Zn-MOF and its derived porous carbon.** The Zn-MOF was synthesized according to the procedure described in previous report<sup>20</sup>. In a typical synthesis process, 2.3 g of benzene-1,4-dicarboxylic acid and 11.9 g of zinc nitrate hexahydrate were dissolved into 160 ml dimethyl formamide (DMF), then transferred into a Teflon-lined stainless steel autoclave. It was then sealed and maintained at 120 °C for 24 h. After filtration and washing by DMF, the Zn-MOF was collected and dried under vacuum at 150 °C overnight. The precursor Zn-MOF was pyrolyzed at 1000 °C in N<sub>2</sub> under atmospheric pressure and vacuum (the furnace pressure was kept

in 0.02–0.04 MPa) to obtain the products, respectively. The sample pyrolyzed under the nitrogen atmosphere at room pressure is named as FPC, and the sample prepared by the vacuum carbonization is marked as VFPC.

**Materials characterization.** Field-emission scanning electron microscopy (FE-SEM; ZEISS SUPRATM 55 field emission microscope), energy-dispersive X-ray spectroscopy (EDS; attached to SEM, Oxford Instruments), X-ray diffraction (XRD; Rigaku D/max-2500B2+/PCX system with  $\text{CuK}\alpha = 1.5406 \text{ \AA}$ ,  $2\theta = 5\text{--}90^\circ$ ) and Raman spectroscopy using a 532 nm laser (Aramis, Jobin Yvon) were carried out to investigate the structure and composition of the samples. Nitrogen sorption isotherms were measured with ASAP2020 (Micromeritics, USA) with a degassed process at 300 °C for 6 h. Specific surface areas were obtained according to the Brunauer-Emmet-Teller (BET) model, and pore size distributions were simulated by the Non-local density functional theory (NLDFT) model. The total pore volume was calculated from the amount adsorbed at  $P/P_0 = 0.994$ .

SAXS experiment was performed using synchrotron radiation as X-ray source at 1W2A station at Beijing Synchrotron Radiation Facility (BSRF). The focused X-ray beam size was about  $1.4 \times 0.2 \text{ mm}^2$  with a flux of  $5.5 \times 10^{11} \text{ phs s}^{-1}$  at 2.5 GeV and 250 mA. Incident X-ray wavelength  $\lambda$  was 0.154 nm. SAXS images were recorded with a Mar 165 CCD detector. The detected intensity is a function of the modulus of the scattering vector  $q = 4\pi \sin\theta/\lambda$ , where  $2\theta$  is the scattering angle, and the obtained results were smeared SAXS data. The calibration of scattering vector was performed involving the incident X-ray wavelength and the sample to detector distance (1608 mm). The normalization and the removal of background were possessed by  $I = I_s - (K_s/K_b)I_b$ , where  $I$  is the processed scattering intensity after background subtraction;  $I_s$  and  $I_b$  are scattering intensity of sample and background, respectively;  $K_s$  and  $K_b$  are the transmitted X-ray intensity of the sample and the background, respectively.

**Electrochemical measurements.** Electrochemical performances were measured by using 2032 coin-type cells with lithium foil as counter electrode. The working electrodes were prepared by pasting the mixtures of 80% active mass, 10% acetylene black and 10% poly (vinylidene difluoride) onto foam nickel. The loading mass of active materials in one working electrode is 2 mg. The electrolyte was a 1 M  $\text{LiPF}_6$  solution in a mixture of ethylene carbonate/dimethyl carbonate (1:1 v/v). The galvanostatical charge-discharge tests were carried out within the potential range of 0.01–3 V vs.  $\text{Li/Li}^+$  at various rates. Electrochemical impedance spectroscopy (EIS) and cyclic voltammetry (CV) measurements of the samples were performed on an electrochemical workstation (CHI 660B). EIS tests were obtained by applying a sine wave with an amplitude of 5.0 mV over the frequency range from 100 kHz to 0.01 Hz. The cyclic voltammograms were obtained over the potential range of 0.01–3 V vs.  $\text{Li/Li}^+$  at a scan rate of  $0.1 \text{ mV s}^{-1}$ .

## References

- Bruce, P. G., Freunberger, S. A., Hardwick, L. J. & Tarascon, J.-M. Li-O<sub>2</sub> and Li-S Batteries with High Energy Storage. *Nat. Mater.* **11**, 19–29 (2011).
- Zheng, F., Yang, Y. & Chen, Q. High Lithium Anodic Performance of Highly Nitrogen-Doped Porous Carbon Prepared from a Metal-Organic Framework. *Nat. Commun.* **5**, 5261 (2014).
- Kashhedikar, N. A. & Maier, J. Lithium Storage in Carbon Nanostructures. *Adv. Mater.* **21**, 2664–2680 (2009).
- Sato, K., Noguchi, M., Demachi, A., Oki, N. & Endo, M. A Mechanism of Lithium Storage in Disordered Carbons. *Science* **264**, 556–557 (1994).
- Liu, Y., Xue, J. S., Tao, Z. J. & Dahn, R. Mechanism of Lithium Insertion in Hard Carbons Prepared by Pyrolysis of Epoxy Resins. *Carbon* **34**, 193–200 (1996).
- Dahn, J. R., Xing, W. & Gao, Y. The “Falling Cards Model” for the Structure of Microporous Carbons. *Carbon* **35**, 825–830 (1997).
- Deschamps, M. & Yazami, R. J. Great Reversible Capacity of Carbon Lithium Electrode in Solid Polymer Electrolyte. *J. Power Sources* **68**, 236–238 (1997).
- Mabuchi, A., Tokumitsu, K., Fujimoto, H. & Kasuh, T. Charge-Discharge Characteristics of The Mesocarbon Microbeads Heat-Treated at Different Temperatures. *J. Electrochem. Soc.* **142**, 1041–1046 (1995).
- Peled, E., Menachem, C., Bar-Tow, D. & Melman, A. Improved Graphite Anode for Lithium-ion Batteries Chemically Bonded Solid Electrolyte Interface and Nanochannel Formation. *J. Electrochem. Soc.* **143**, L4–L7 (1996).
- Vu, A., Qian, Y. & Stein, A. Porous Electrode Materials for Lithium-Ion Batteries: How to Prepare Them and What Makes Them Special. *Adv. Energy Mater.* **2**, 1056–1085 (2012).
- Roberts, A. D., Li, X. & Zhang, H. Porous Carbon Spheres and Monoliths: Morphology Control, Pore Size Tuning and Their Applications as Li-Ion Battery Anode Materials. *Chem. Soc. Rev.* **43**, 4341–4356 (2014).
- Lee, J. *et al.* Recent Progress in the Synthesis of Porous Carbon Materials. *Adv. Mater.* **18**, 2073–2094 (2006).
- Fang, B., Kim, J. H., Kim, M. S. & Yu, J. S. Hierarchical Nanostructured Carbons with Meso-Macroporosity: Design, Characterization, and Applications. *Acc. Chem. Res.* **46**, 1397–406 (2012).
- Fu, R. W. *et al.* Hierarchical Porous Carbons: Design, Preparation, and Performance in Energy Storage. *New Carbon Mater.* **26**, 171–179 (2011).
- Trogadas, P., Ramani, V., Strasser, P., Fuller, T. F. & Coppins, M. O. Hierarchically Structured Nanomaterials for Electrochemical Energy Conversion. *Angew. Chem. Int. Ed.* **55**, 122–148 (2016).
- Chaikittisilp, W., Ariga, K. & Yamauchi, Y. A New Family of Carbon Materials: Synthesis of MOF-Derived Nanoporous Carbons and Their Promising Applications. *J. Mater. Chem.* **1**, 14–19 (2013).
- Lux, L., Williams, K. & Ma, S. Heat-Treatment of Metal-Organic Frameworks for Green Energy Applications. *CrystEngComm*, **17**, 10–22 (2015).
- Zhang, H., Zhou, Y. & Song, X. Advanced Functional Materials Derived from Metal-Organic Frameworks. *Prog. Chem.* **27**, 174–191 (2015).
- Salunkhe, R. *et al.* Asymmetric Supercapacitors Using 3D Nanoporous Carbon and Cobalt Oxide Electrodes Synthesized from a Single Metal-Organic Framework. *ACS nano*, **9**, 6288–6296 (2015).
- Banerjee, A. *et al.* MOF-Derived Crumpled-Sheet-Assembled Perforated Carbon Cuboids as Highly Effective Cathode Active Materials for Ultra-High Energy Density Li-Ion Hybrid Electrochemical Capacitors (Li-HECs). *Nanoscale*, **6**, 4387–4394 (2014).
- Zhang, P., Sun, F., Shen, Z. & Cao, D. ZIF-Derived Porous Carbon: A Promising Supercapacitor Electrode Material. *J. Mater. Chem.* **2**, 12873–12880 (2014).
- Klose, M. *et al.* Hollow Carbon Nano-Onions with Hierarchical Porosity Derived from Commercial Metal Organic Framework. *Carbon*, **79**, 302–309 (2014).

23. Xu, G. *et al.* Sulfur Embedded in Metal Organic Framework-Derived Hierarchically Porous Carbon Nanoplates for High Performance Lithium-Sulfur Battery. *J. Mater. Chem. A*, **1**, 4490–4496 (2013).
24. Zhao, S. *et al.* Carbonized Nanoscale Metal-Organic Frameworks as High Performance Electrocatalyst for Oxygen Reduction Reaction. *ACS nano*, **8**, 12660–12668 (2014).
25. Hu, H., Han, L., Yu, M., Wang, Z. & Lou, X. W. D. Metal-Organic-Framework-Engaged Formation of Co Nanoparticle-Embedded Carbon@Co<sub>9</sub>S<sub>8</sub> Double-Shell Nanocages for Efficient Oxygen Reduction. *Energy Environ. Sci.* **9**, 107–111 (2016).
26. Ma, T. Y., Dai, S., Jaroniec, M. & Qiao, S. Z. Metal-Organic Framework Derived Hybrid Co<sub>3</sub>O<sub>4</sub>-Carbon Porous Nanowire Arrays as Reversible Oxygen Evolution Electrodes. *J. Am. Chem. Soc.* **136**, 13925–13931 (2014).
27. Zhang, G. *et al.* High-Performance and Ultra-Stable Lithium-Ion Batteries Based on MOF-Derived ZnO@ZnO Quantum Dots/C Core-Shell Nanorod Arrays on a Carbon Cloth Anode. *Adv. Mater.* **27**, 2400–2405 (2015).
28. Li, H., Liang, M., Sun, W. & Wang, Y. Bimetal-Organic Framework: One-Step Homogenous Formation and its Derived Mesoporous Ternary Metal Oxide Nanorod for High-Capacity, High-Rate, and Long-Cycle-Life Lithium Storage. *Adv. Funct. Mater.* **26**, 1098–1103 (2016).
29. Shen, C., Zhao, C., Xin, F., Cao, C. & Han, W. Q. Nitrogen-Modified Carbon Nanostructures Derived from Metal-Organic Frameworks as High Performance Anodes for Li-ion Batteries. *Electrochim. Acta.* **180**, 852–857 (2015).
30. Huang, G. *et al.* Metal Organic Frameworks Route to *in Situ* Insertion of Multiwalled Carbon Nanotubes in Co<sub>3</sub>O<sub>4</sub> Polyhedra as Anode Materials for Lithium-Ion Batteries. *ACS Nano*, **9**, 1592–1599 (2015).
31. Liang, H. W., Zhuang, X., Brüller, S., Feng, X. & Müllen, K. Hierarchically Porous Carbons with Optimized Nitrogen Doping as Highly Active Electrocatalysts for Oxygen Reduction. *Nat. Commun.* **5**, 4973 (2014).
32. Li, Z. H. A Program for SAXS Data Processing and Analysis. *Chin. Phys. C*, **37**, 108002 (2013).
33. Ehrburger-Dolle, F. *et al.* Nanoporous Carbon Materials: Comparison Between Information Obtained by SAXS and WAXS and by Gas Adsorption. *Carbon*, **43**, 3009–3012 (2005).
34. Schmidt, P. W. Small-Angle Scattering Studies of Disordered, Porous and Fractal Systems. *J. Appl. Crystallogr.* **24**, 414–435 (1991).
35. Arico, A. S., Bruce, P., Scrosati, B., Tarascon, J. M. & Van Schalkwijk, W. Nanostructured Materials for Advanced Energy Conversion and Storage Devices. *Nat. Mater.* **4**, 366–377 (2005).
36. Wang, Y. *et al.* Multifunctional Carbon Nanostructures for Advanced Energy Storage Applications. *Nanomaterials*, **5**, 755–777 (2015).
37. Yang, Z. *et al.* Recent Advancement of Nanostructured Carbon for Energy Applications. *Chem. Rev.* **115**, 5159–5223 (2015).
38. Koberstein, J. T., Morra, B. & Stein, R. S. The Determination of Diffuse-Boundary Thicknesses of Polymers by Small-Angle X-Ray Scattering. *J. Appl. Crystallogr.* **13**, 34–45 (1980).
39. Teixidor, G. T., Park, B. Y., Mukherjee, P. P., Kang, Q. & Madou, M. J. Modeling Fractal Electrodes for Li-Ion Batteries. *Electrochim. Acta*, **54**, 5928–5936 (2009).
40. Park, B. Y., Zaouk, R., Wang, C. & Madou, M. J. A Case for Fractal Electrodes in Electrochemical Applications. *J. Electrochem. Soc.* **154**, P1–P5 (2007).

## Acknowledgements

The part of this work was supported by the National Natural Science Foundation of China (51672021, 51572014, 51272019, U1332107 and U1532105). Z.L. thanks the financial support of State Key Laboratory for Coal Resources and Safe Mining, China University of Mining & Technology (SKLRCRM14KFA02). H.L. acknowledges the partial funding support from Argonne National Laboratory. Argonne, a U.S. Department of Energy Office of Science laboratory, is operated under Contract No. DE-AC02-06CH11357.

## Author Contributions

A.L. and H.S. designed this research. A.L. carried out the experiments and data analysis, and wrote the manuscript. Y.T. assembled the coin-type cells for battery tests. B.C. prepared the figures and scheme. Z.L. performed the SAXS tests and provided the computer program S for SAXS data processing. X.C., J.Z., G.C. and H.L. helped for the sample measurements. All authors contributed to the scientific discussion and manuscript revisions.

## Additional Information

**Supplementary information** accompanies this paper at <http://www.nature.com/srep>

**Competing financial interests:** The authors declare no competing financial interests.

**How to cite this article:** Li, A. *et al.* MOF-derived multifractal porous carbon with ultrahigh lithium-ion storage performance. *Sci. Rep.* **7**, 40574; doi: 10.1038/srep40574 (2017).

**Publisher's note:** Springer Nature remains neutral with regard to jurisdictional claims in published maps and institutional affiliations.



This work is licensed under a Creative Commons Attribution 4.0 International License. The images or other third party material in this article are included in the article's Creative Commons license, unless indicated otherwise in the credit line; if the material is not included under the Creative Commons license, users will need to obtain permission from the license holder to reproduce the material. To view a copy of this license, visit <http://creativecommons.org/licenses/by/4.0/>

© The Author(s) 2017